

Optimal Time-Series Selection of Quasars

Nathaniel R. Butler¹ & Joshua S. Bloom^{2,3}

ABSTRACT

We present a novel method for the optimal selection of quasars using time-series observations in a single photometric bandpass. Utilizing the damped random walk model of Kelly et al. (2009), we parameterize the ensemble quasar structure function in Sloan Stripe 82 as a function of observed brightness. The ensemble model fit can then be evaluated rigorously for and calibrated with individual light curves with no parameter fitting. This yields a classification in two statistics — one describing the fit confidence and one describing the probability of a false alarm — which can be tuned, *a priori*, to achieve high quasar detection fractions (99% completeness with default cuts), given an acceptable rate of false alarms. We establish the typical rate of false alarms due to known variable stars as $\lesssim 3\%$ (high purity). Applying the classification, we increase the sample of potential quasars relative to those known in Stripe 82 by as much as 29%, and by nearly a factor of two in the redshift range $2.5 < z < 3$, where selection by color is extremely inefficient. This represents 1875 new quasars in a 290 deg^2 field. The observed rates of both quasars and stars agree well with the model predictions, with $> 99\%$ of quasars exhibiting the expected variability profile. We discuss the utility of the method at high redshift and in the regime of noisy and sparse data. Our time-series selection complements well independent selection based on quasar colors and has strong potential for identifying high-redshift quasars for BAO and other cosmology studies in the LSST era.

Subject headings: quasars: general — stars: variables: other — methods: statistical — cosmology: miscellaneous

¹Einstein Fellow, Astronomy Department, University of California, Berkeley, CA, 94720-7450, USA

²Astronomy Department, University of California, Berkeley, CA, 94720-7450, USA

³Sloan Research Fellow

1. Introduction

Active Galactic Nuclei (AGN) — and quasars (QSOs) in particular — continue to play a central role in modern astrophysics. AGN emission is the hallmark of supermassive black hole growth. Powerful AGN outflows of photons and matter affect the Universe on small (accretion disk) and large (galactic, extragalactic) size scales, and there is now substantial evidence both from observations and simulations (both semi-analytical and hydrodynamical) that a “quasar mode” is a key part of massive galaxy formation and evolution. On an ensemble basis, the observed number densities (e.g., Croom et al. 2009), large scale-structure (e.g., Shen et al. 2007, 2009; Ross et al. 2009), and use as cosmological probes via the Lyman- α forest and Baryon Acoustic Oscillations (BAO; e.g., McDonald & Eisenstein 2007), demonstrate that luminous AGN — despite their rare nature — provide elucidating constraints on some of the grandest questions of our time.

To fully exploit the potential of active galaxies, astronomers must identify and characterize the physics of large, representative samples. Recent surveys have identified quasars using spectroscopy (e.g., Schneider et al. 2010), color-selection (e.g., Richards et al. 2009), X-ray detections (e.g., Bauer et al. 2004), and optical variability (e.g., Schmidt et al. 2010), among other methods. The quasar catalogs generated by these surveys exhibit a range of different completeness and efficiency characteristics. This is partly due to differences in telescope sensitivities for the different surveys, but also to intrinsic differences in the physics that each survey samples. Deep X-ray surveys and optical variability surveys currently show the most promise for identifying large numbers of AGN per square degree of sky (Brandt & Hasinger 2005).

Optical surveys most often utilize quasar photometric colors to separate quasars from field stars. Typical “completeness” fractions — the fraction of retained spectroscopically-confirmed quasars — for the selection of quasars based on color are $\gtrsim 70\%$ (e.g., Richards et al. 2001), although this can decrease dramatically, to $10 - 50\%$, in the redshift range ($2.5 < z < 3$) where the quasar UV color excess ($u-g$ color) is similar to that of stars (Richards et al. 2006) or for highly extinguished quasars. The “purity” of selection, or the fraction of false alarms due to spectroscopically-confirmed stars, can be similarly low. Optical variability provides an independent selection criteria and is becoming an increasingly important survey technique. Quasar selection based on optical variability is a key component of current and upcoming missions, such as the Panoramic Survey Telescope & Rapid Response System (PanSTARRS; Kaiser et al. 2002) and the Large Synoptic Survey Telescope (LSST; Ivezić et al. 2008; Abell et al. 2009). Indeed, with the recent endorsement by the Astro2010 Decadal Survey of both ground and space-based wide-field synoptic surveys, exploring discovery in the time domain is particularly timely.

Quasar fluxes observed in optical passbands (e.g., Matthews & Sandage 1963) meander in time, non-periodically, with flux differences that tend to be larger on larger timescales (e.g., Hook et al. 1994). This has historically been characterized in studies of auto-correlation using the so-called “structure function” (e.g., Simonetti, Cordes & Heeschen 1985; Hughes, Aller & Aller 1992), evaluating the average square variations versus timescale for an ensemble of quasars. It is generally assumed that the combination of observations from individual sources, each perhaps observed only a pair or a few times, will accurately describe the intrinsic variability of a given quasar. Data from the Sloan Digital Sky Survey (SDSS; e.g., Abazajian et al. 2009), and high-time-cadence observations for Stripe 82¹ in particular, have allowed major advances in quantifying and understanding the nature of this variability (e.g., Vanden Berk 2004; Ivezić et al. 2004), particularly for individual objects (e.g., MacLeod et al. 2010; Sesar et al. 2010). We explore in detail below the connection between the ensemble variability and the variability of individual, well-sampled quasars.

The correlated variability of quasars is unique compared to most other variable objects (e.g., stars) which tend on long-timescales (e.g., long relative to a periodicity timescale) to exhibit non-correlated variability. Quasars tend to vary much less on monthly and shorter timescales as compared to yearly timescales, unlike most stars (excluding, e.g., long-period variables). This distinction motivates the possibility of using quasar time series modelling to classify quasar and differentiate them from other objects. Such a classification, particularly if it can be done efficiently, with few data, could have tremendous benefit for selecting quasars for spectroscopic followup and use in cosmological studies (e.g., of BAO; McDonald & Eisenstein 2007). Progress towards these ends is now becoming possible thanks to the generative “damped random walk” quasar light curve model — a model capable of stochastically producing a quasar like light curve, in this case with only 2 input parameters — uncovered by Kelly et al. (2009). Kozłowski & Kochanek (2010) have shown that this model accurately describes the light curves of 100 well-sampled quasars, and it can be used to separate these from stars. MacLeod et al. (2010) have shown that the model accurately describes individual quasars in Stripe 82. We show that it can be used to accurately describe the ensemble variability as well as the individual variability.

Below, we discuss a novel method to fit the structure function for Stripe 82 using the damped random walk model (Section 2). We then show (Section 3) how the fit of this average quasar model can be rigorously evaluated for individual light curves to separate quasars from stars with no parameter fitting. We show that nearly all known quasars ($> 99\%$; Section 4) in

¹The equatorial Stripe 82 region ($20^{\text{h}} 24^{\text{m}} < \text{R.A.} < 04^{\text{h}} 08^{\text{m}}$, $-1.27^{\circ} < \text{Dec} < +1.27^{\circ}$, $\sim 290^{\circ}$ deg²) was repeatedly observed — 58 imaging runs from 1998 September to 2004 December — with 1–2 observations per week, each Fall.

Stripe 82 show the telltale variability signature, with a very high completeness ($\approx 99\%$) that can be estimated a-priori. This offers a substantial improvement over ad-hoc methods (e.g., 90% completeness in Schmidt et al. 2010) for applying structure function fits to individual light curves. The fraction of stars which could be confused as quasars is, likewise, very small ($< 3\%$) and is in reasonable agreement with *a-priori* estimates.

The method we outline below is based on maximum likelihood principles; it is therefore theoretically optimal and applicable to any field or survey. The quasar probabilities returned by the method robustly take into account model uncertainties and uncertainties (both statistical and systematic) in the data. The method can be applied in the limit of very few data points (2 or more), because there are no free parameters to fit and can provide key additional leverage to aid color-based selection schemes for future surveys. The methodology is easily adaptable to include observations in multiple photometric filters and to avoid contamination from spurious data.

2. Data Selection and Ensemble Quasar Variability

The majority of work presented herein makes use of the *ugriz* photometry from the Sesar et al. (2007) variable source catalog. That catalog contains 67,507 $g < 20.5$ objects in Sloan Stripe 82. These are selected based on the presence of statistically significant temporal variability (> 0.05 mag RMS and $\chi^2_\nu/\nu > 3$ in g and r). Additional details regarding the survey selection criteria can be found in Sesar et al. (2007). The variability selection retains $\gtrsim 90\%$ of known (spectroscopic) quasars in the field. Those spectroscopically identified quasars were almost all entirely targeted as a result of color selection from the main SDSS survey (and not because of time-domain characteristics).

Our goal is to differentiate quasars from other field sources using variability metrics alone, without regard to color or cross-correlation with surveys at other wavebands. We begin by evaluating the ensemble variability of 6304 spectroscopically-confirmed quasars in Sesar et al. (2007) to quantify the observed range of magnitude change, Δmag , as a function of timescale $\tau_{ij} = t_i - t_j$ between measurements at times t_i and t_j .

Figure 1 shows a histogram of all magnitude differences in g -band for measurements separated on timescales τ (in days) between $1.5 < \log(\tau) < 1.8$. The histogram is apparently symmetric, peaked at zero, and has broad, exponential wings. The exponential distribution here is commonly found (e.g., Ivezić et al. 2004). We find that the histogram can be well modelled as a sum of zero-mean Gaussians whose widths scale logarithmically with the quasar magnitude. Residual non-Gaussianity (i.e., an excess of large fluctuations as compared to

the predictions from a Gaussian) is due to a small fraction (2%) of sources with excess variability (see also, Section 5.2). Figure 2 plots the Gaussian width — after removing the measurement uncertainty — as a function of magnitude and τ . This is commonly known as the first order quasar structure function $SF_\tau = \sigma_{\Delta\text{mag}(\tau)}$ (e.g., Simonetti, Cordes & Heeschen 1985; Hughes, Aller & Aller 1992).

To move from the ensemble variability to the variability of a given object, it is necessary to treat the covariances between neighboring points — which are estimated from the same data — in the structure function. Given the approximate Gaussianity of the ensemble, it is natural to fit a Gaussian random process to individual objects. Consistent with previous works (Kelly et al. 2009; Kozłowski & Kochanek 2010; MacLeod et al. 2010), we find that the quasar variability as a function of time difference is well-modelled using a covariance matrix of the form:

$$C_{ij} = \sigma_i^2 \delta_{ij} + \frac{1}{2} \hat{\sigma}^2 \tau_o \exp(-\tau_{ij}/\tau_o), \quad (1)$$

where σ_i is the measurement uncertainty for the i 'th observation, τ_o is an exponential damping timescale (units of days), $\hat{\sigma}^2$ is the intrinsic variance between observations on short timescales $\tau_{ij} \approx 1$ day, and δ_{ij} is the Kronecker delta function (1 for $i = j$, 0 otherwise). This model predicts $SF_\tau \propto \hat{\sigma} \tau_o^{1/2} [1 - \exp(-\tau_{ij}/\tau_o)]^{1/2}$, which rises $\propto \tau_{ij}^{1/2}$ on short timescales ($\tau_{ij} \ll \tau_o$). This model is plotted over the data in Figure 2. To obtain an acceptable fit, we allow $\hat{\sigma}^2$ and τ_o to vary logarithmically with the median quasar magnitude. The best fit scalings for the *ugriz* bands are reported in Table 1. Python software to calculate the fits and the quality statistics discussed below can be downloaded from the project webpage².

²http://astro.berkeley.edu/~nat/qso_selection

Table 1: Structure Function Parametrization

| Filter | a_1 | a_2 | a_3 | a_4 |
|----------|-------|-------|-------|-------|
| <i>u</i> | −3.90 | 0.12 | 2.73 | −0.02 |
| <i>g</i> | −4.10 | 0.14 | 2.92 | −0.07 |
| <i>r</i> | −4.34 | 0.20 | 3.12 | −0.15 |
| <i>i</i> | −4.23 | 0.05 | 2.83 | 0.07 |
| <i>z</i> | −4.44 | 0.13 | 3.06 | −0.07 |

Notes: $SF_\tau = \hat{\sigma} \tau_o^{1/2} [1 - \exp(-\tau/\tau_o)]^{1/2}$, with $\log(\hat{\sigma}^2) = a_1 + a_2(\text{mag} - 19)$, $\log(\tau_o) = a_3 + a_4(\text{mag} - 19)$. Statistical uncertainties in the above parameters are of order 10^{-4} and are negligible. Magnitudes are in the AB system, uncorrected for Galactic extinction.

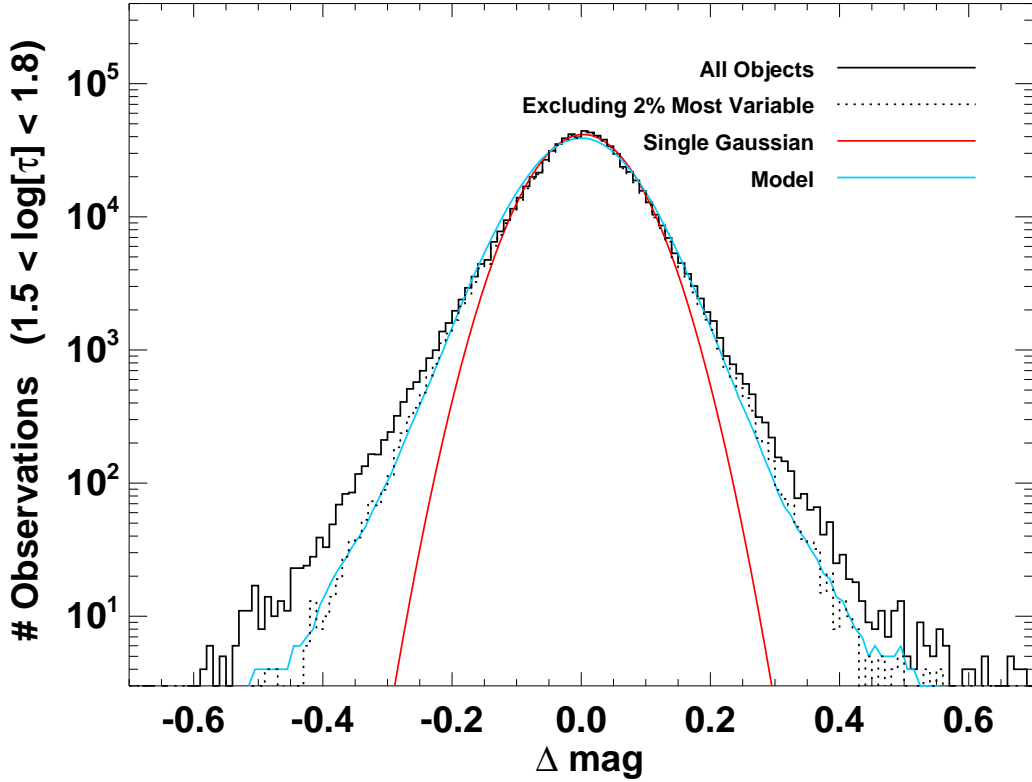


Fig. 1.— The histogram of magnitude differences in g -band observed for 6304 quasars on timescales $10^{1.5} < \tau < 10^{1.8}$ days. This is a time range which is particularly well-sampled for Stripe 82. The distribution has broader wings than a Gaussian (red curve); however it is well-represented by the superposition of Gaussian’s (blue curve) with widths that increase logarithmically (Table 1) with the quasar magnitude. Residual non-Gaussianity can be attributed to a fraction 2% of quasars which exhibit excess variability.

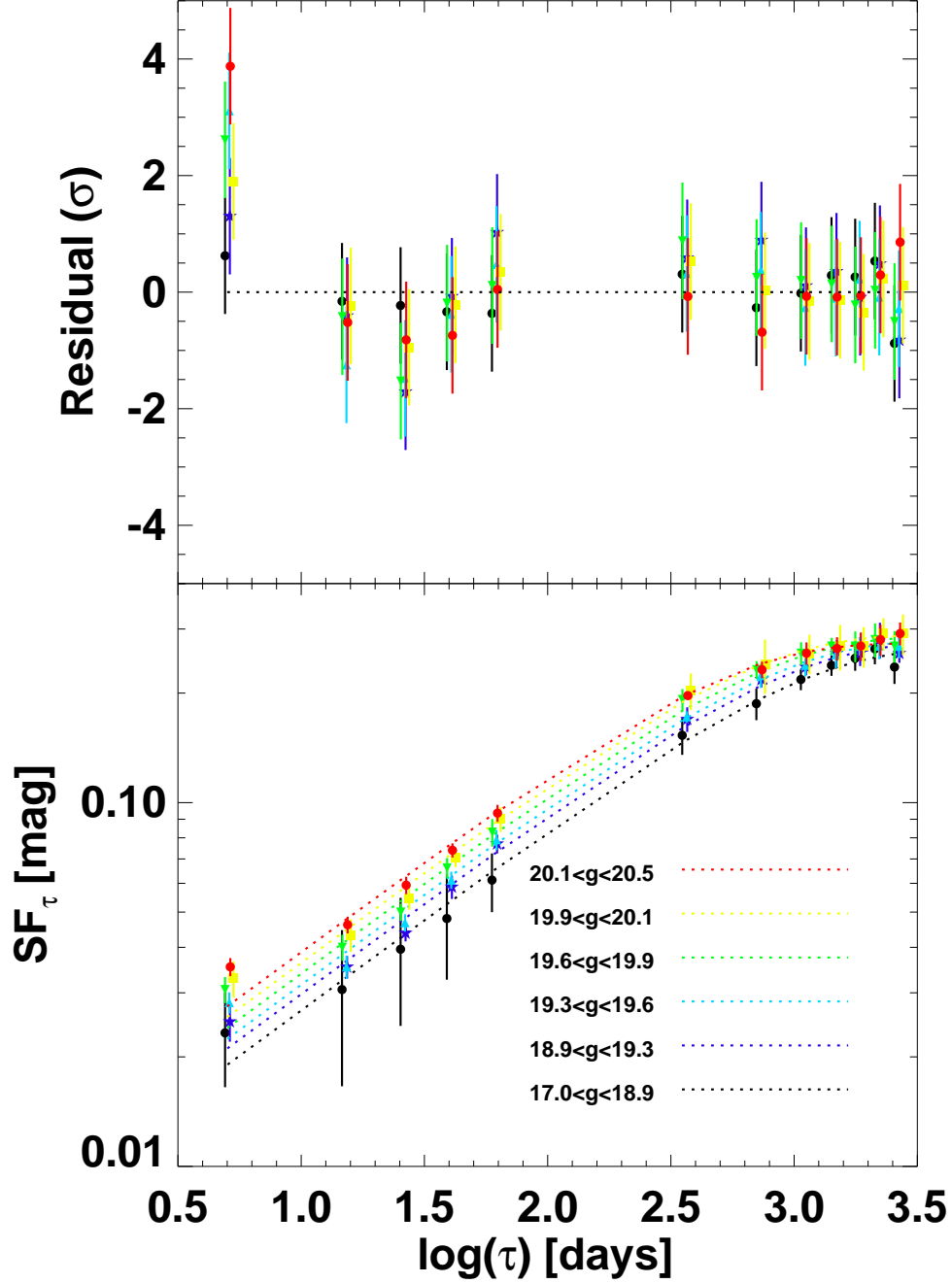


Fig. 2.— The ensemble structure function SF_τ for quasars in SDSS Stripe 82 in g -band. Each bin corresponds to a set of order 10^4 difference measurements. The maximum likelihood Gaussian variance in addition to the measurement uncertainty is determined for each pair, and the median and standard deviation of these values for each set is plotted. The data points are well-fit (dotted curves) by the damped random walk model (see text) with parameters that vary with quasar magnitude only to reproduce the observed increase in variability for faint sources (Table 1). There is modest evidence (shortest timescale points) for untreated systematic measurement uncertainty at the $\lesssim 1\%$ level.

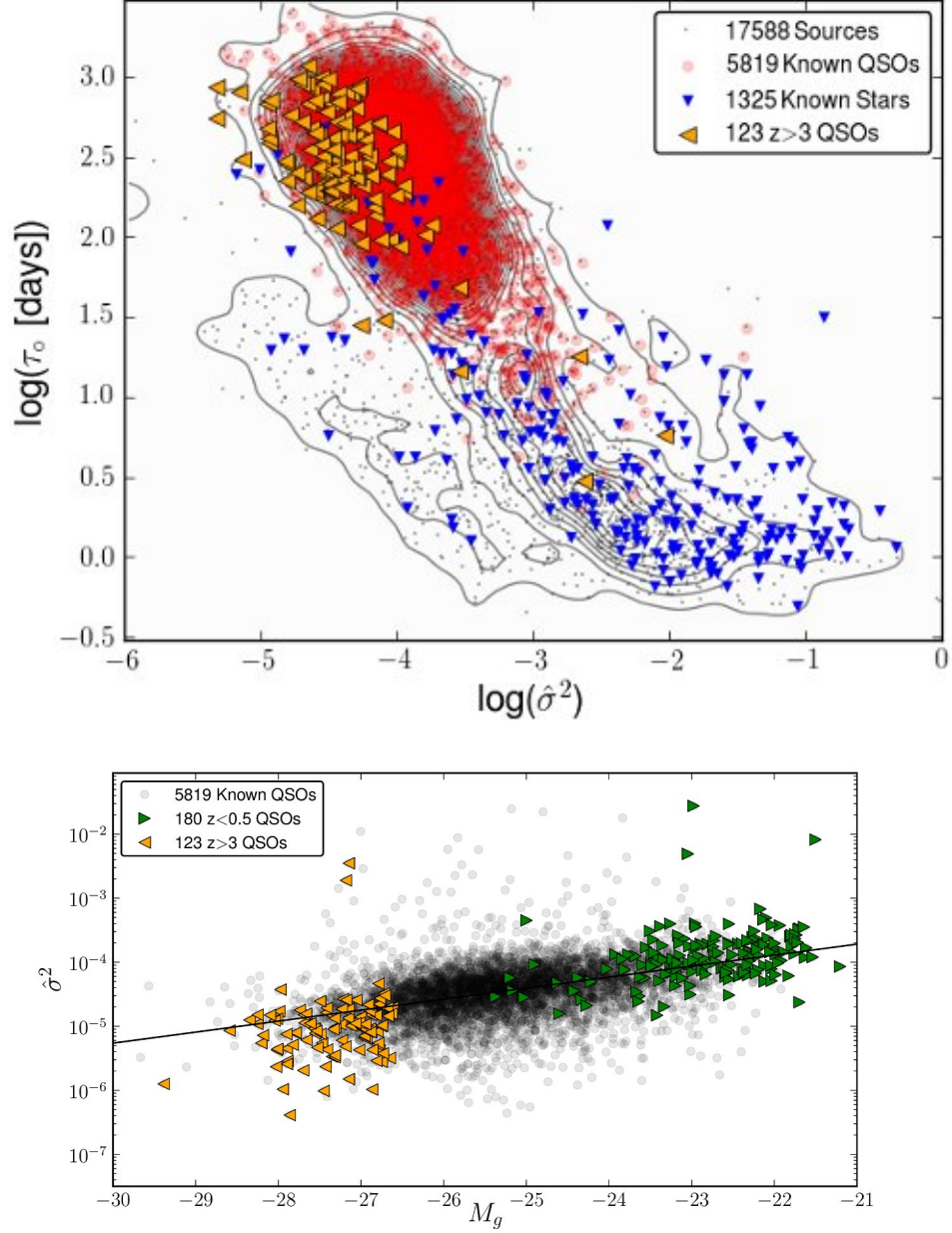


Fig. 3.— (A) Exponential damping timescale τ_o for the random walk SF_τ model versus the short-timescale variance $\hat{\sigma}^2$. Spectroscopically-confirmed quasars appear in the top left of the plot, while spectroscopically identified stars appear in the bottom right. High redshift ($z > 3$) quasars tend to have weak, short-timescale variability (see text). (B) The short-timescale variability scales with intrinsic brightness $\log(\hat{\sigma}^2) = 0.17G - 0.1$, with large scatter. High redshift objects appear toward the left due to the survey flux limit $g < 20.5$. Low redshift objects appear toward the right. Typical uncertainties are ± 1 dex in τ_o and $\hat{\sigma}^2$ (90% confidence).

We can also fit the SF_τ model directly by maximizing the posterior probability of the model given the data (see, also, Kozłowski & Kochanek 2010). The best-fit $\hat{\sigma}^2$ and τ_o values for each quasar are plotted in Figure 3A for g band. Note that consistent scalings with the g band magnitude (Table 1) are found.

The origin of the scaling of variability with source brightness appears to stem from the well-known anti-correlation between intrinsic brightness and variability (e.g., Ivezić et al. 2004). Figure 3B displays this trend for the absolute magnitude in g -band, M_g . We note that $\hat{\sigma}^2$ no longer correlates with g -band magnitude or redshift after subtracting away this trend. High-redshift quasars tend to appear toward the left of the plot (Figure 3B) — weak short-timescale variability — due to the $g = 20.5$ flux limit. The effects of a declining luminosity function (and potentially source evolution) also work to keep low-redshift objects toward the right of the plot. The normalization of the fit in Figure 3B can be seen to vary slightly with redshift also as a result of this flux limit, and we can expect the apparent magnitude scalings (Table 1) to also have some dependence on redshift and the survey selection (see, Section 5.3). These shifts are small compared to the (apparently intrinsic) ~ 1 dex scatter in the scalings (e.g., Figure 3B).

3. Quasar Variability Selection Formalism

We can regard the parameterization of the SF_τ using the damped random walk model as a rigorous mathematical approach to evaluating the quasar likelihood for a given light curve, which takes into account all correlations in the data. Employing the mathematical prescription adapted from Rybicki & Press (1994) by Kozłowski & Kochanek (2010), we write for the probability of the data x given the quasar variance model $C = C(\hat{\sigma}^2, \tau_o)$:

$$P(x|\hat{\sigma}^2, \tau_o) \propto |C|^{-1/2} \exp[-0.5(x - x_o)^T C^{-1}(x - x_o)]. \quad (2)$$

We can marginalize analytically over x_o and replace the exponent in Equation 2 with

$$-0.5\chi_{\text{QSO}}^2 = -0.5(x - x_{o,\text{best}})^T C^{-1}(x - x_{o,\text{best}}), \quad (3)$$

where $x_{o,\text{best}} = \sum_{i,j} C_{ij}^{-1} x_j / \sum_{i,j} C_{ij}^{-1}$. The inverse of C is tridiagonal (Rybicki & Press 1994), which allows for rapid $O(N)$ computation. Given the parameterization above (Table 1) for τ_o and $\hat{\sigma}^2$ in terms of apparent magnitude mag , we can then directly evaluate $\chi_{\text{QSO}}^2(\text{mag})$ for all objects of interest with no additional fitting (i.e., no fitting beyond the fitting of x_o).

For a quasar with the mean ensemble variability, χ_{QSO}^2 should be χ_ν^2 distributed with ν degrees of freedom, where ν equals the number of data points minus one. The most likely value is $\chi_{\text{QSO}}^2 = \nu$. The expected distribution of χ_{QSO}^2 for a temporally-uncorrelated source can be evaluated by Monte Carlo or estimated quickly as we now discuss.

3.1. Significance Estimates

The expected value for χ_{QSO}^2 for a source that is not a quasar but varies in a time-independent fashion with Gaussian scatter σ_m is

$$E[\chi_{\text{QSO}}^2] \approx E[x^2] \text{Tr}(C^{-1}) \equiv \sigma_m^2 \text{Tr}(C^{-1}), \quad (4)$$

where $E[x]$ is the expectation value of x and $\text{Tr}()$ is the matrix trace operation. In Equation 4, we assume that all observations have approximately the same uncertainty, and we ignore the light curve mean. Because off-diagonal terms in C^{-1} do not contribute, χ_{QSO}^2 in Equation 4 is effectively a sum of the squares of N Gaussian random variables — each with zero mean and standard deviation σ_m , which includes the measurement uncertainty — multiplied by a constant, $\text{Tr}(C^{-1})/N$. Therefore, the quantity $N\chi_{\text{QSO}}^2/[\sigma_m^2 \text{Tr}(C^{-1})]$ will be χ_ν^2 distributed, where the number of degrees of freedom $\nu = N - 1$. (The missing degree of freedom represents the light curve mean which we have neglected to write down).

The true value of σ_m^2 must be determined from the data. In the case again of equal uncertainty on all data points,

$$P(\sigma_m^2|x) \propto \sigma_m^{-N} \exp(-0.5Nv_x/\sigma_m^2), \quad (5)$$

where $v_x \equiv \langle x^2 \rangle - \langle x \rangle^2$. Multiplying the χ_ν^2 probability density for $N\chi_{\text{QSO}}^2/[\sigma_m^2 \text{Tr}(C^{-1})]$ by $P(\sigma_m^2|x)$ and integrating over σ_m , we find a Beta distribution for the Null-hypothesis distribution of χ_{QSO}^2 given the data:

$$P(\chi_{\text{QSO}}^2|x, \text{not quasar}) \propto (y[1-y])^{(\nu-1)/2}, \quad (6)$$

with $y \equiv \chi_{\text{QSO}}^2/[\chi_{\text{QSO}}^2 + v_x \text{Tr}(C^{-1})]$. This reference distribution approximates well the observed χ_{QSO}^2 frequencies for stars (Figure 6) and can be used as the reference distribution to calculate the significance of a given χ_{QSO}^2 value. It is useful also to define

$$\chi_{\text{False}}^2/\nu \equiv \frac{v_x \text{Tr}(C^{-1})}{\chi_{\text{QSO}}^2} \quad (7)$$

The quantity χ_{False}^2 will be small and of order ν for a time-independent, non-quasar variable source (i.e., a potential false alarm).

3.2. Confidence Estimates

As we discuss above, the χ_{QSO}^2 calculated for a hypothetical mean quasar — varying according to Equation 1 with the best-fit parameters in Table 1 defining $\hat{\sigma}^2$ and τ_o — will

be of order $\nu = N - 1$ and χ_{QSO}^2 will follow a χ_ν^2 distribution. However, the variability of a given quasar may depart from the mean sample variability. We can allow for this on a source-by-source basis by replacing $C \rightarrow C/s^2$ in Equation 2. The scale factor s is a fudge factor that can be marginalized over to allow the mean quasar model to acceptably fit each quasar light curve.

The distribution of s given the data for a given quasar is given by Equation 5, replacing σ_m with s and Nv_x with the most likely value for χ_{QSO}^2 of ν . In an argument parallel to that above used to derive significance, the χ_ν^2 probability density describing χ_{QSO}^2/s^2 can be convolved with $P(s^2|x)$ to find a reference Beta distribution to evaluate quasar confidence:

$$P(\chi_{\text{QSO}}^2|x, \text{quasar}) \propto (y'[1 - y'])^{(\nu-1)/2}, \quad (8)$$

with $y' \equiv \nu/[\nu + \chi_{\text{QSO}}^2]$. Likewise for $P(\chi_{\text{QSO}}^2|x, \text{not quasar})$ for stars, this reference distribution approximates well the observed χ_{QSO}^2 frequencies for quasars (Figure 6).

Note that because the reference distribution for evaluating significance has the same form as that used to evaluate confidence, a curve of constant $\chi_{\text{QSO}}^2/\chi_{\text{False}}^2$ represents a curve of equal odds in favor of the hypothesis quasar versus not-quasar, given equal prior information.

4. Quasar Variability Selection Application

In addition to 6573 quasars from Schneider et al. (2010), 3020 labelled stars (i.e., spectroscopically-confirmed) in the DR7 are plotted in Figure 3A. We note that the total number of objects now known to be quasars and used in these plots (and those below) is larger than the quasar sample of 6307 from Sesar et al. (2007) used above to establish SF_τ . Known stars tend to have $\tau_o \lesssim 100$ days (i.e., approximately temporally-uncorrelated variability) and also increased variability on short timescales relative to quasars (see, also, MacLeod et al. 2010). In principle, Figure 3A can be used for classification of unlabeled sources as well (e.g., Kozłowski & Kochanek 2010); however, we and others find the uncertainties in these parameters to be large (often a factor of ten even for well-observed sources). Also, there is significant overlap between the populations of labelled sources. A more optimal separation could be developed by seeking to fit no free parameters.

Figure 4 shows χ_{QSO}^2 and χ_{False}^2 for all 17,588 sources in Sesar et al. (2007) with 50 or more observations in g -band. Roughly 70% of all sources in Stripe 82 — excluding $290 < \text{R.A.} < 340$ degrees where the Galactic stellar contribution dominates the source counts and blending between sources becomes common — have 50 or more observations. There is a clear separation between the majority of stars and quasars, and the values of χ_{QSO}^2 and χ_{False}^2 take on their expected values for labelled sources. For the population cut shown in Figure

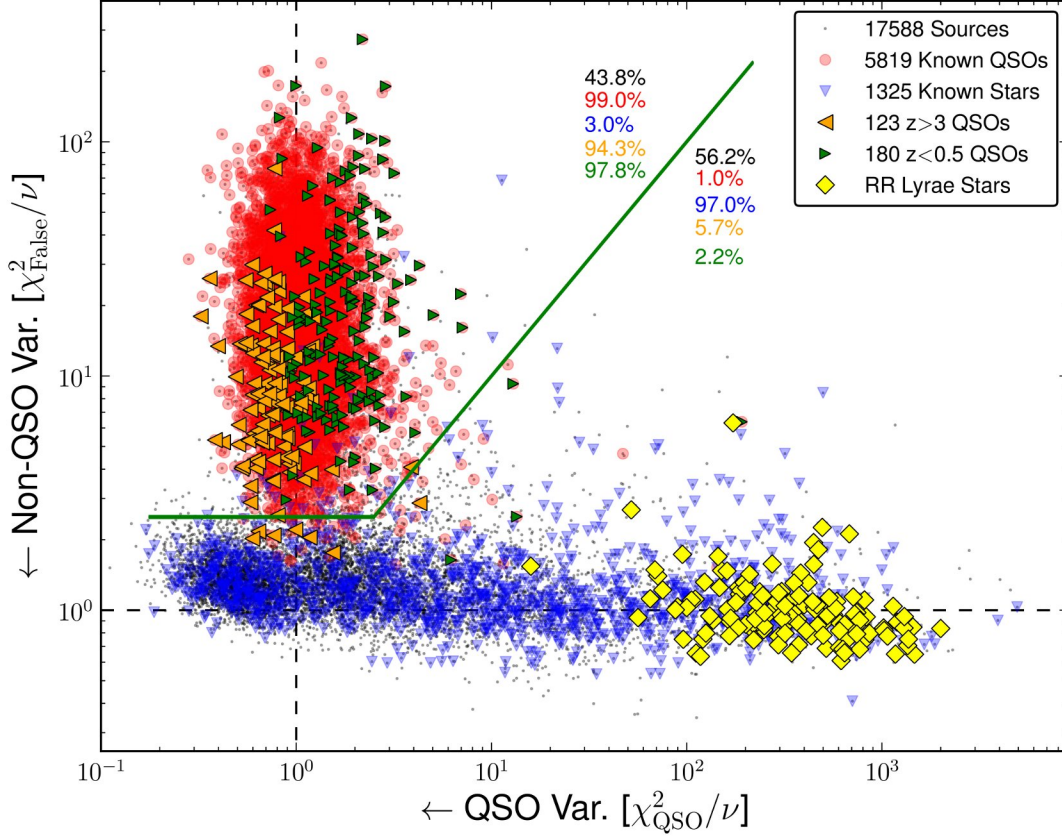


Fig. 4.— Non-quasar variability metric χ^2_{False} versus quasar-like variability metric χ^2_{QSO} for g -band observations of sources with > 50 epochs in Sesar et al. (2007). Spectroscopically confirmed quasars (from Schneider et al. 2010) and stars are marked in red and blue, respectively. The low ($z < 0.5$) and high ($z > 3$) redshift quasars are additionally marked in green and orange, respectively, to display the trend toward low variability at high- z . The solid line (highlighted in green) represents a cut based on equal probability ($\chi^2_{\text{QSO}} = \chi^2_{\text{False}}$) between the hypotheses. There is also a cut on $\chi^2_{\text{False}} > 2.5$, corresponding to a $\gtrsim 3.5\sigma$ significance cut (Section 3.1) against false positives. RR Lyrae stars (from; Sesar et al. 2010), which are highly variable, are also plotted as yellow diamonds. The percentages of objects on either side of the cut are recorded in the figure (descending in the same order as in the legend).

4, the completeness fraction for the fraction of known quasars retained is 99%. One minus the fraction of known stars retained, the purity, is 97%.

Of all sources, we predict that 40% are quasars, potentially increasing the overall known quasar sample size by 20%. The candidate quasars have a distribution in g -band magnitude consistent with that of the known quasars. We discuss the newly discovered quasars in more detail below in Section 5.

We also show explicitly in the plots the location of low redshift ($z < 0.5$) and high redshift ($z > 3$) quasars, 97.8% and 94.3% of which, respectively, survive the nominal quasar selection. These tend to have systematically high and low χ^2_{QSO} values, respectively, due to the trend toward low variability at high luminosity discussed above.

The selection can be optimized to pursue $z > 3$ quasars by placing a more stringent cut on $\chi^2_{\text{QSO}}\nu < 2$ (low quasar-like variability) to reduce the number of selected low-redshift quasars and also relaxing the cut on overall variability to allow in more false alarms, $\chi^2_{\text{False}}/\nu > 2$. The resulting completeness (purity) for selecting $z > 3$ quasars is 97.6% (95.7%), considering only contamination by stars (95% of $z < 3$ quasars are retained, but most could be rejected using color information; Figure 8). Two of the three high-redshift quasars that do not survive the refined χ^2_{QSO} cut can be retained using the outlier rejection scheme outlined below. (These quasars both have a single deviant photometric point.)

The classification defined by the cut in Figure 4 essentially assumes equal prior probability that a source is or is not a quasar (Section 4). We can see (Figure 5) that the classification remains quite stable over a broad range of source densities which include the high stellar-density region of $290 < \text{R.A.} < 340$ (degrees) and also now include sources with few measurement epochs (the minimum in the Sesar et al. (2007) sample is 9). Because we are now classifying sources with few observation epochs, we select based on the significance level of a given χ^2_{False} rather than on simply χ^2_{False} . The completeness (purity) we derive for Figure 5 is 99.1% (97.1%), relatively little changed. However, we caution that this neglects the fact that few sources are spectroscopically identified at high source densities $\rho \gtrsim 10^3 \text{ deg}^{-2}$ (R.A. ≈ 300 degrees). It is clear that the dramatic rise in the overall source counts — which must be dominated by stars — would lead to marked completeness and purity decreases. It is, therefore, advisable in such high source density regions to apply a more strict cut on χ^2_{False} . In principle, prior information on the expected source density in a given direction for a given survey should be utilized to dial in an appropriate threshold value.

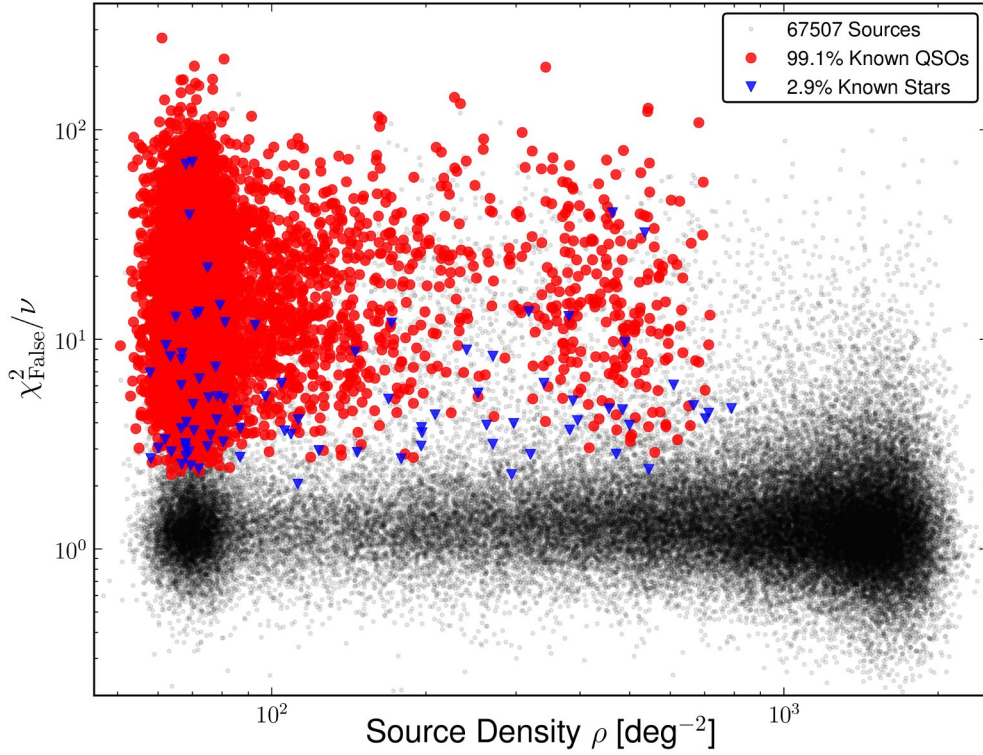


Fig. 5.— The non-quasar variability metric versus source density ρ for all sources ($N \geq 9$ epochs per source). Known quasars and stars that survive a $> 3.5\sigma$ significance cut on χ^2_{False} and also have $\chi^2_{\text{QSO}} < \chi^2_{\text{False}}$ to be classified as quasars are plotted in red and blue, respectively. The classification — which assumes equal prior probability that a given source is or is not a quasar (Section 4) — is quite stable over a broad range in ρ . At very high $\rho \gtrsim 10^3 \text{ deg}^{-2}$ there are few spectroscopic identifications and the stellar population begins to envelope the quasar population, demanding a higher level significance cut.

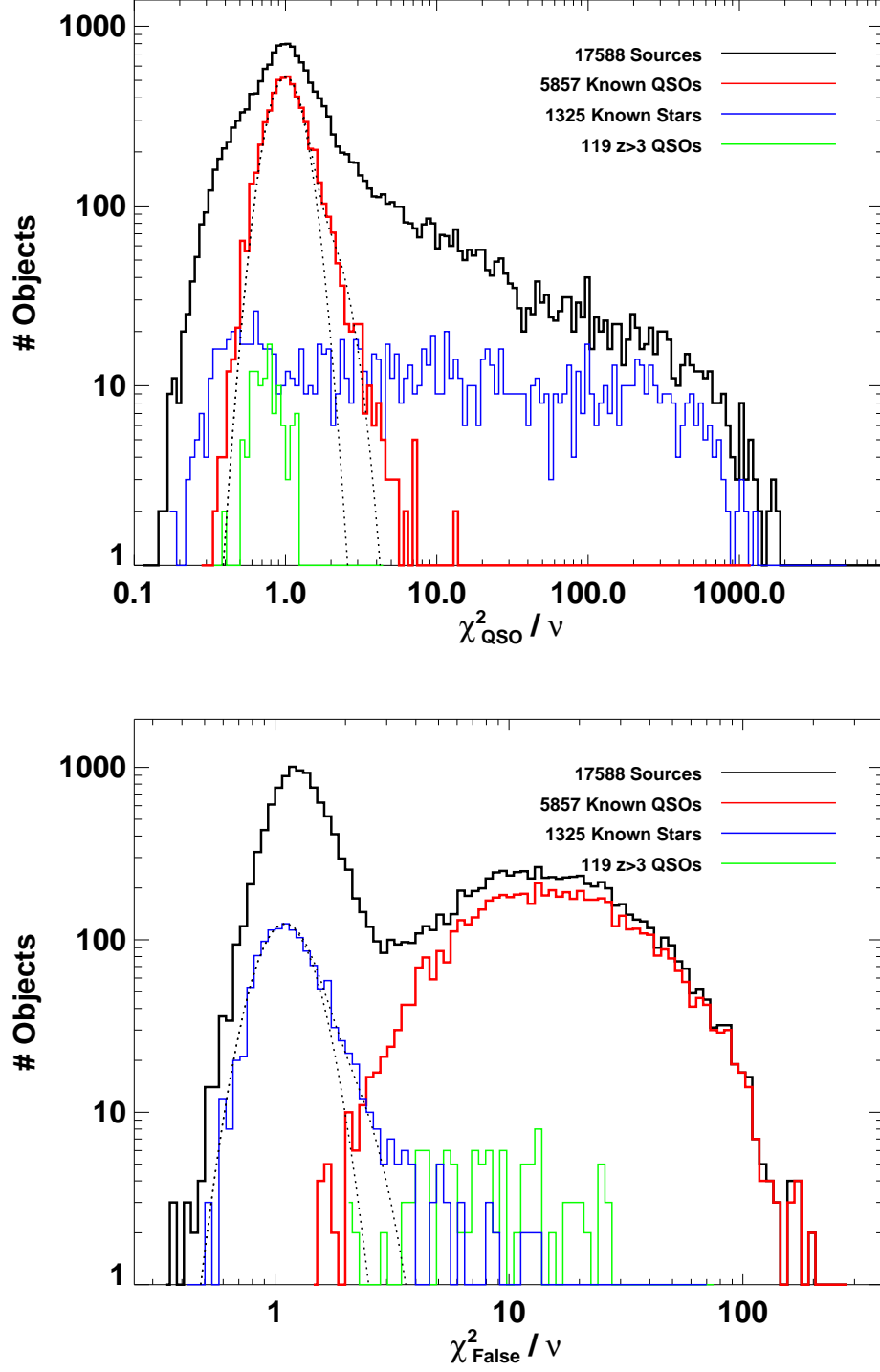


Fig. 6.— Projections of the axes in Figure 4 for χ^2_{QSO}/ν (top) and $\chi^2_{\text{False}}/\nu$ (bottom). The dotted curves show the predicted Beta distributions for the source counts (see text), including an excess of variable objects in both plots at the $\lesssim 10\%$ level.

4.1. Significance/Confidence Validation: Tail Populations

Figure 6 shows the observed distributions of χ_{QSO}^2 and χ_{False}^2 . Over-plotted are the expected Beta distributions (Section 4) for the median number of degrees of freedom $\nu = 55$. These describe the observed frequencies well, apart from a tail of 10% of variable stars which have $\chi_{\text{False}}^2/\nu \approx 2$ on average and a tail of 10% of highly-variable quasars which have $\chi_{\text{QSO}}^2/\nu \approx 2$ on average. These tail contributions can be used to obtain a precise significance estimate and rates which agree well with predictions, although this improvement has little impact on the logarithmic quasar/star separation in Figure 4. We note that 50% of the $\chi_{\text{QSO}}^2/\nu > 2$ objects are at low redshift ($z < 1$), where our approximation that variability scales as apparent (instead of absolute) magnitude is expected to break down.

Taking into account the excess number of events in the tails of the observed χ_{QSO}^2 and χ_{False}^2 distributions (Figures 6), a cut on either parameter at a value of 2.5 (corresponding to $\approx 3.5\sigma$ without the tail estimates) would need to be increased to ≈ 4.1 to account for the tails at the same significance level. This corresponds to a $\approx 5\sigma$ cut on the initial distributions, ignoring the tails. Therefore, a conservative prescription to either reject false positives or to reject quasars, respectively, is to cut on χ_{False}^2 or χ_{QSO}^2 , respectively, at the 5σ significance level. At this significance level, there are few outliers: 26 stars ($\approx 1\%$ of the sample) masquerading with $\chi_{\text{QSO}}^2 < \chi_{\text{False}}^2$ as quasars and 15 ($\approx 0.3\%$ of the sample) of overly-variable quasars, after excluding quasars at $z < 1$. We discuss the nature of these strong outliers in Section 5.2 below.

5. Discussion

The light curve fitting above has the potential to provide vital information for quasar selection, particularly for those objects which are challenging to select based on their photometric colors. Figure 7 shows the location of all Sesar et al. (2007) objects in the $u - g, g - r$ color plane. Low redshift quasars tend to lie in a tight locus to the left of the plot. Stars run along a branch upward and to the left. High redshift (and also potentially highly extinguished) quasars fan out to the right of the quasar locus, through the stellar region. Color-based selection is clearly challenging for these objects (see also, Richards et al. 2006). We show in Figure 8 that our method is capable of identifying a substantial number — 1875 in this case — of highly statistically significant quasar candidates. Very few of these ($\approx 1\%$) lie in the color-color space typically dominated by stars (Region ‘V’ in Figure 7), and we suspect some of these 26 candidates are extinguished quasars.

The selection for Figure 8 synthesizes recommendations from above. For the high-

Galactic latitude portion of Stripe 82 (excluding $290 < \text{R.A.} < 340$ degrees), we apply a 5σ cut on χ^2_{False} to eliminate the tail of variable stars (Section 5.2; Figure 6, bottom). A higher significance cut (7σ) is utilized for the low-Galactic latitude region to account for the higher stellar density (Figure 5). Finally, we ignore sources brighter than $i = 18$ (corresponding to $\approx 3\%$ of the known quasar sample but likely few of the candidate quasar sample). This cut also helps to eliminate bright, red sources (i.e., primarily late-type stars at $g - r \gtrsim 1.3$, $u - g \gtrsim 2$ in Figure 7), which are almost certainly not quasars.

Quasars redshifts correlate strongly with their colors; three regions (A, B, and C) which contain $\gtrsim 90\%$ of quasars in the redshift ranges $z \lesssim 2.5$, $2.5 \lesssim z \lesssim 3$, and $z \gtrsim 3$, respectively, are plotted in Figure 8. These regions are defined so as to maintain the total number of quasars per redshift bin associated with a given color-color bin. Table 2 displays the number of known, spectroscopic quasars in each color bin as well as the number of new candidate quasars discovered here. In the last two columns of the table, we make this comparison separately for the bright ($i \leq 19$ mag) and faint ($i > 19$ mag) samples. In parentheses in these columns, we quote the implied fractional increase in known quasars.

We potentially increase the overall known quasar sample by 29% (1875/6573), with a substantial contribution (+89%) in the color-color region (B) where color selection is most difficult. The number of known $z \gtrsim 3$ quasars would increase by 36–46%, depending upon whether we include 15 candidate quasars located in the stellar region V in Figure 7. These gains are primarily due the selection here of the faint ($i > 19$ mag) quasars, although the fractional increases for $z \gtrsim 3$ quasars are relatively independent of source brightness. It is important to note when making these comparisons that these gains are relative to *spectroscopically-confirmed* quasars, whereas a large number of our candidates (1280) are also (un-observed) candidates based on color (Richards et al. 2006). The fraction of new

Table 2: Redshift Counts from Candidate Quasars Colors

| Color Region | # Known | New (% Known) | New $i \leq 19$ | New $i > 19$ |
|-----------------------------------|---------|----------------------------|--------------------------|----------------------------|
| A ($z \lesssim 2.5$) | 6086 | 1498, <i>297</i> (25%, 5%) | 93, <i>44</i> (6%, 3%) | 1405, <i>253</i> (30%, 6%) |
| B ($2.5 \lesssim z \lesssim 3$) | 325 | 288, <i>230</i> (89%, 71%) | 43, <i>41</i> (58%, 55%) | 245, <i>189</i> (98%, 75%) |
| C ($z \gtrsim 3$) | 140 | 65, <i>48</i> (46%, 33%) | 13, <i>11</i> (43%, 37%) | 52, <i>37</i> (47%, 34%) |

Notes: The color regions A, B, and C are defined in the text and in Figure 7. Columns 3–5 report the number of new quasars relative to spectroscopically-confirmed quasars, followed after a comma by the number (italicized) of new quasars not already color-selected in Richards et al. (2009) or spectroscopically-confirmed.

quasars relative to color-selected quasars are quoted as the second percentage in the final two columns of Table 2. These numbers suggest that color-based selection is complete at the $\gtrsim 95\%$ level below $z \approx 2.5$ and rather incomplete at higher redshift.

As most of the new quasar candidates come from the faint end of the detected source population, where the color selections are more incomplete (owing in part to the need for high signal-to-noise imaging in multiple filters), it is tempting to restrict to the brighter sources in making a direct comparison of time-domain and color selection completeness and purity; Table 2 provides this. However, viewing the entirety of Stripe 82 as a fixed volume of data, the fact that high-confidence quasars can be obtained fainter than the color-selection limit might be considered legitimate advantage of our technique.

Table 3 gives the number of known and candidate sources corresponding to the 6 color-color regions discussed in Sesar et al. (2007). These regions define the typical color-color locations of various astrophysical transients (see, Figure 7). The relative frequencies of the candidate quasars falling within a given region are roughly consistent with those of the known quasars. We note that there is a marked, relative increase in the number of candidates possibly associated with stellar locus stars (region V) and RR Lyrae stars (region IV). RR Lyrae stars tend to be strongly rejected as quasar candidates (Figure 4). In future work we will further explore what fraction of candidate quasars in the stellar locus are stars or highly extinguished quasars.

5.1. Weakly Variable or Non-Variable Quasars?

Sesar et al. (2007) determine that 93% of spectroscopically-confirmed quasars brighter than $g, r = 19.5$ in Stripe 82 are variable at the > 0.03 mag level. They report a conservative fraction ($> 90\%$), which is limited by the measurement uncertainty. Fitting a detailed model for the expected variability, we can make a more general statement regarding the fraction of quasars that vary. As reported above, $> 99\%$ of quasars with 50 or more data points yield a highly significant χ^2_{False} . The quasar population dwindles strongly below $\chi^2_{\text{False}}/\nu = 2.5$ (a 3.5σ cut on variability), unlike the stellar population. The majority of stars have $\chi^2_{\text{False}} \approx \nu$ which can occur either because the variability is not qso-like or because the variability simply is not statistically significant beyond the measurement error.

The fact that nearly all quasars brighter than $g = 20.5$ have $\chi^2_{\text{False}}/\nu > 2.5$ (99.1% of quasars including those with as few as 9 measurement epochs; Section 4) indicates an intrinsic variability at least 60% larger than the typical measurement error of 0.02 mag. Quasars with weaker variability can be measured, and they are missing from Figure 4. The

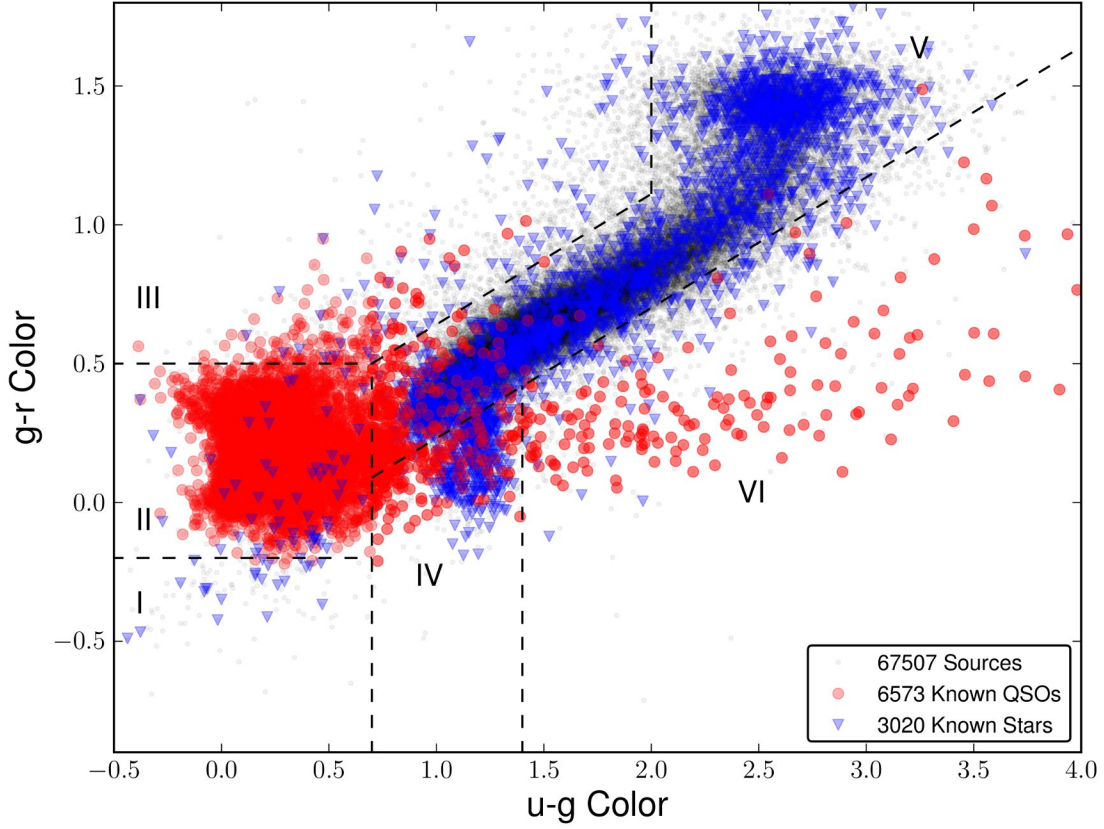


Fig. 7.— Color-color plot showing the location of spectroscopically-confirmed stars (blue triangles) and quasars (red circles). All of the sources from Sesar et al. (2007) are plotted as small black dots. We demarcate with dashed lines the regions which Sesar et al. (2007) find to contain, primarily, white dwarves (I), low-redshift quasars (II), dM/WD pairs (III), RR Lyrae stars (IV), stellar locus stars (V), and high-redshift quasars (VI).

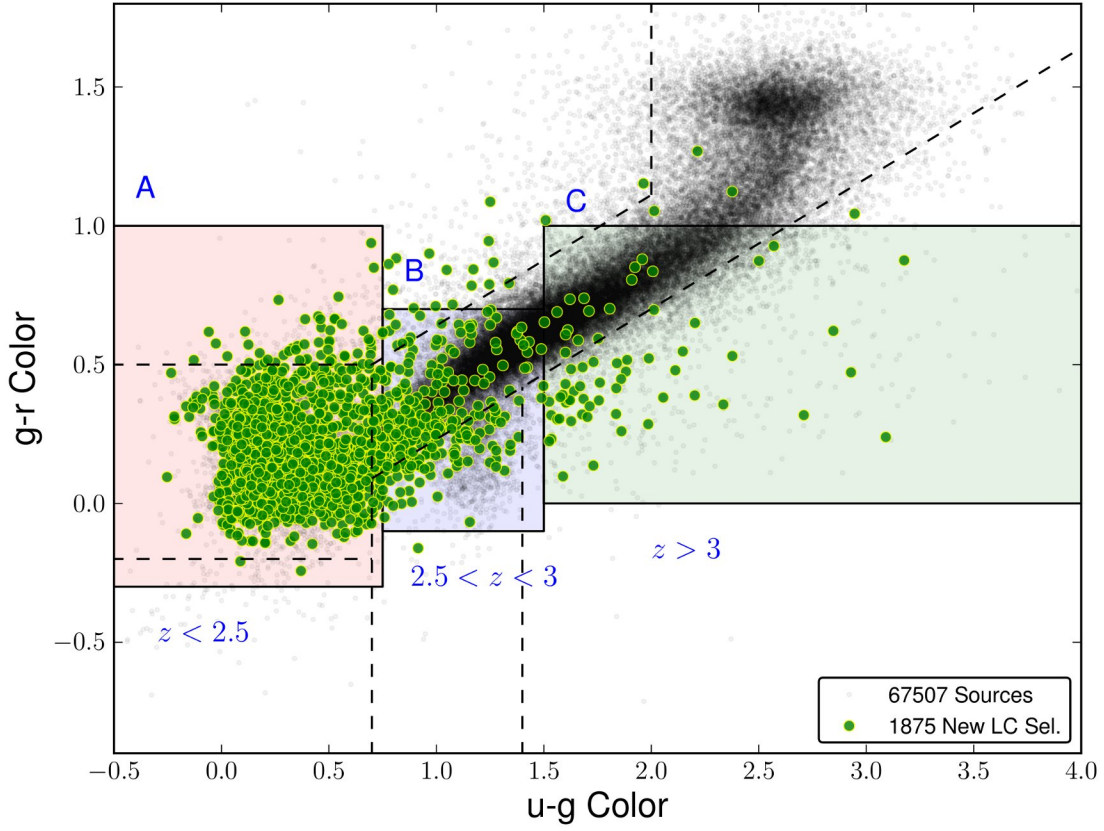


Fig. 8.— Color-color plot showing the location of all sources from Sesar et al. (2007) in black (small dots). We plot in green (circles) the location of 1875 new quasar candidates with significances $> 5\sigma$, $> 7\sigma$ for $290 < \text{R.A.} < 340$ (degrees). Labelled are the color-color regions A,B, and C, corresponding to quasars lying approximately in the redshift ranges $z < 2.5$, $2.5 < z < 3$, and $z > 3$, respectively. Also plotted are the dashed-line demarcations from Figure 7.

variability cut in Sesar et al. (2007) is agnostic as to whether a source is truly a quasar; therefore the presence of weakly variable stars where no weakly variable quasars are found (in Figure 4) indicates that approximately all quasars are intrinsically variable.

Using the spectroscopic sample from Schneider et al. (2010), in addition to the 6537 quasars considered above which have light curves as part of the Sesar et al. (2007) project, there are 505 which are not contained in the Sesar et al. (2007) sample. We downloaded³ the light curves for these quasars. The extra fraction of potential quasars reflects uncertainty in the overall sample size (due, e.g., to cuts on deblending flags, etc.). We find that 35 of 285 sources with more than 8 measurement epochs yield $\chi^2_{\text{False}}/\nu < 2.5$. Only 9 of these have sufficiently weak variability to not be rejected as stable by a classical χ^2_ν test at the $> 5\sigma$ level. This confirms that the fraction of non-variable quasars is very small ($\lesssim 1\%$) and not impacted strongly by the Sesar et al. (2007) variability selection.

5.2. Outliers

We have visually inspected the light curves and spectra for the strong outliers (26 stars and 15 quasars) identified above. Two-thirds of the quasar outliers appear to be the result of a mild amount of errant photometry: we note the $\chi^2_{\text{QSO}} \approx \nu$ when calculated in r band for these objects and $\chi^2_{\text{QSO}} \approx \nu$ also in g -band provided we remove 1–3 outlying (by $> 5\sigma$) flux measurements. This outlier identification for individual points in a quasar light curve is determined using the prediction for data point x_i given all the other data points (see, e.g., Kozłowski & Kochanek 2010, or our software²). Of the remaining five sources, two have poor photometry apparently as the result of deblending from a nearby bright source and two have only marginally large χ^2_{QSO} after accounting for outliers. We retain one objects (SDSS J001130.40+005751.7), a ROSAT source which appears to truly exhibit excessive, particularly short-timescale, variability ($\chi^2_{\text{QSO}}/\nu > 30$, $\tau_o \approx 10$ days, in this case) as compared to the remaining sample of ≈ 6000 .

Vanden Berk (2004) find evidence for a significant increase in short-timescale variability for ROSAT-associated quasars. Consistently, we find a mild increase in χ^2_{QSO} on average for 94 ROSAT-associated quasars in Schneider et al. (2007). Of these, 80% have $\chi^2_{\text{QSO}} > \nu$, and the median is $\chi^2_{\text{QSO}}/\nu = 1.5$. All but a few of these are at $z < 1$, which suggests the poor quasar fit quality is due to the standard luminosity dependent variability (Figure 3B) and not an anomalously high intrinsic variability. MacLeod et al. (2010) have also looked at this

³Using an SQL query on the Stripe 82 database hosted by SDSS at http://cas.sdss.org/stripe82/en/tools/search/x_sql.asp

issue and find no statistically significant difference in variability for Stripe 82 quasars in the context of the damped random walk model.

An effective scheme for rejecting outliers from an individual quasar light curve, which retains the separation between quasars and stars in Figure 4, can be implemented as follows. First and foremost, apply no outlier rejection in calculating χ_{False}^2 . Next, choose a maximum allowed number of outliers (say 3) and a significance level for the residual (say 5σ). Calculate χ_{QSO}^2 and the model prediction for the light curve to evaluate outliers iteratively, each time removing only the strongest outlier. Once this is complete, evaluate the standard deviation of the residuals and repeat the process with a significance cutoff that is the larger of 5 or 5 times the standard deviation. This two-step process makes it so that non-quasars receive little outlier rejection.

We note that the calculation of χ_{QSO}^2 with this outlier rejection scheme substantially dampens by a factor ≈ 2 the tail of 10% of mild outlying quasars, leaving primarily only the low- z quasars/AGN. The peak in χ_{QSO}^2 also shifts down by about 10% for all quasars. We note that we do not utilize this outlier rejection in the paper because the χ_{QSO}^2 tails are adequately small in our view. Some form of outlier rejection may be quite important when using less pristine photometry.

The outlier rejection method summarized above is tailored for quasars and has no effect on the tail of 26 strongly outlying stars in χ_{False}^2 or the 10% tail of modestly outlying stars. Of these objects, only 4 are late-type stars (which could, in principle be rejected based on color as discussed above). Seven of the objects have quasar-like colors (Figure 7), have targeting flags in SDSS associated with quasars, and have low-confidence ($< 95\%$ at best) redshift determinations. We regard these as potentially mis-labeled stars. Fifteen high-confidence stars remain, and nine (about 0.3% of the full sample) exhibit quasar-like ($\chi_{\text{QSO}}^2/\nu < 2$) variability. We note that one of these objects was targeted as a white dwarf (SDSS J234601.89–004255.5), and in a future study we will probe in more detail the nature of the other outliers and the potential that the underlying physics (e.g., the presence of an accretion disk) may be similar to that of quasars.

The data from multiple filters can also be combined to obtain more robust values for χ_{QSO}^2 and χ_{False}^2 . The average of these for g and r bands leads to a small, but significant, improvement in the separation in Figure 4. (The addition of other bands helps little.) To eliminate outliers in the case of approximately simultaneous data, it may also be effective to throw out observation epochs exhibiting strong color variations, for example > 5 times the standard deviation away from the median color $g - r$. We observe that the quasar colors are relatively stable in neighboring photometric bands as a function of time, although there is a mild dependence on redshift. There are $\approx 30\%$ color variations that occur — presumably

due the difference in continuum and line variability — for redshifts that place the $\lambda = 2800\text{\AA}$ MgII line (also, Ivezić et al. 2004) in one of the passbands.

We have explored also simultaneously fitting Equation 2 to the data from 2 or more passbands to potentially improve statistics. One way to do this is to use the covariance matrix (Equation 1) for the data from one reference passband (e.g., g -band) and then to allow the other bands to only vary linearly with the g -band magnitude. We find that the g and r band data can be fit-well in this fashion, which further indicates the approximate constancy of quasar $g - r$ colors. However, the statistics (as measured by the scatter and source separation in Figure 4) do not improve.

5.3. Redshift Estimation

In Figures 3B and 4 above, we show a tendency for increased variability with decreasing luminosity which maps to a trend of decreasing variability with redshift. The survey flux limit plays a role in this trend, and evolutionary effects are also likely at work. Our classification appears to perform best above $z = 1$ as a result. In principle, the classification can be further optimized to identify bursts at higher redshift (see, e.g., Figure 4) by performing a strict cut on χ_{QSO}^2 (see, Section 4).

It is also possible to estimate the redshift of a quasar using either $\hat{\sigma}^2$ or χ_{QSO}^2 . The scatter in $1 + z$ estimated this way relative to the true $1 + z$ is large, a factor of 2. There are also likely strong selection effects at play. The flux limit prevents high redshift bursts from exhibiting strong variability. That is, the Malmquist (1922) bias induces a time-domain bias. The survey color-based selection may also play a role. We caution the reader that selection effects that define a given survey may also strongly impact the utility of this redshift estimation. It is not clear at present that useful redshift constraints can be obtained from our variability measures.

6. Conclusions

We have explored a parameterization of the ensemble quasar variability structure function using the damped random walk model (Kelly et al. 2009). This enables a statistically rigorous evaluation of the fit of an individual quasar to the expected sample average variability profile. The latter step provides, essentially, a classification between objects undergoing quasar-like variability and objects exhibiting temporally uncorrelated variability. Unlike previous work, the classification requires no parameter fitting, is essentially free from survey-

specific peculiarities, and appears to be very robust in separating known variable stars from quasars. Nearly all ($> 99\%$) known quasars show the expected variability profile and can be cleanly separated from stars, with $\lesssim 3\%$ contamination by rare variable stars.

Our variability-selected quasar candidates span a range of redshifts, including a factor of nearly two increase in rates for intermediate redshifts ($2.5 < z < 3$), where color-based selection performs poorly (e.g., Richards et al. 2006). The classification performs well also at high-redshift, and can be tuned to yield $> 98\%$ completeness for $z > 3$ quasars. We potentially increase the sample of quasars in Stripe 82 by 10–25%, depending upon whether we compare to color-selected (but not spectroscopically-confirmed) quasars or to spectroscopically-confirmed quasars only. Most of the new quasars are faint ($i > 19$ mag). Relatively independent of these considerations, we increase the quasar fraction by 33% or more for $z \gtrsim 2.5$. Software to perform the classification as well as the list of candidate quasars can be downloaded from the project webpage².

This work has been conducted under the auspices of a broader project (The Time-domain Classification Project; Bloom et al. 2008), a goal of which is to characterize the allowed range of variability versus timescale for the full diversity of astrophysical objects. We have shown above how the temporal profile of quasars stands out against the signature of variable stars, predominantly on long timescales but with strong power to separate strong variables from quasars on short timescale. Future work will apply the methods outlined above to select highly extinguished and high-redshift quasars for spectroscopic followup and also to embed the methods discussed above within the broader TCP framework of variable object classification. Of particular interest will be additional tests of schemes (outlined above) to reject photometric outliers and to apply the classification in the limit of very few data points for wide-field, and in particular real-time surveys, for example using data from the Palomar Transients Factory (Rau et al. 2009).

The “one-versus-many” classification framework shown here should prove to be an important pillar of any survey that relies on time-domain photometric observations for target selection (even if the targets of interest are not quasars). It appears that with the appropriate selection of cadences, the time-domain identification of quasars is now more robust, complete and pure compared with color selections. This has important implications for survey strategies of LSST, the Synoptic All-Sky Infra-Red survey (SASIR; Bloom et al. 2009), and other time-domain projects (e.g., WFIRST): when faced with a choice between more colors and a wider field in a given filter, the latter option is preferred. With deep imaging in one blue band (U or g), coupled with synoptic imaging in a redder band, we believe that high-redshift quasars may be most effectively discovered.

NRB is supported through the Einstein/GLAST Fellowship Program (NASA Cooperative Agreement: NNG06DO90A). JSB was supported by a grant from the National Science Foundation (“Real-time Classification of Massive Time-series Data Streams”; Award #941742).

We acknowledge John Rice, Dovi Poznanski, Nic Ross, Željko Ivezić, Chelsea MacLeod, Berian James, David Schlegel, Chris Kochanek, and Gordon Richards for useful conversations. We also thank an anonymous referee for excellent comments and suggestions which improved the manuscript. We thank B. Sesar et al. for their excellent SDSS variable source catalog. Funding for the SDSS and SDSS-II has been provided by the Alfred P. Sloan Foundation, the Participating Institutions, the National Science Foundation, the U.S. Department of Energy, the National Aeronautics and Space Administration, the Japanese Monbukagakusho, the Max Planck Society, and the Higher Education Funding Council for England. The SDSS Web Site is <http://www.sdss.org/>. The SDSS is managed by the Astrophysical Research Consortium for the Participating Institutions. The Participating Institutions are the American Museum of Natural History, Astrophysical Institute Potsdam, University of Basel, University of Cambridge, Case Western Reserve University, University of Chicago, Drexel University, Fermilab, the Institute for Advanced Study, the Japan Participation Group, Johns Hopkins University, the Joint Institute for Nuclear Astrophysics, the Kavli Institute for Particle Astrophysics and Cosmology, the Korean Scientist Group, the Chinese Academy of Sciences (LAMOST), Los Alamos National Laboratory, the Max-Planck-Institute for Astronomy (MPIA), the Max-Planck-Institute for Astrophysics (MPA), New Mexico State University, Ohio State University, University of Pittsburgh, University of Portsmouth, Princeton University, the United States Naval Observatory, and the University of Washington.

REFERENCES

- Abazajian, K. N., et al. 2009, *ApJS*, 182, 543
- Abell, P. A., et al. 2009, *arXiv:0912.0201*
- Bauer, F. E., et al. 2004, *AdSpR*, 34, 2555
- Bloom, J. S., et al. 2008, *Astr. Nach.*, 329, 284
- Bloom, J. S., et al. 2010, *arXiv:0905.1965*
- Brandt, W. N., & Hasinger, G. 2005, *ARA&A*, 43, 827

- Croom, S. M., et al. 2009, MNRAS, 399, 1755
- Hook, I. M., et al. 1994, MNRAS, 268, 305
- Hughes, P. A., Aller, H. D., Aller, M. F. 1992, ApJ, 396, 469H
- Ivezić, Ž., et al. 2004, IAU Symposium 222, T. Storchi-Bergmann, L.C. Ho, & H. R. Schmitt eds.
- Ivezić, Ž., et al. 2008, arXiv:0805.2366
- Kaiser, N., et al. 2002, SPIE 4836, 154
- Kelly, B. C., et al. 2009, ApJ, 698, 895
- Kozłowski, S., & Kochanek, C. S. 2010, ApJ, 708, 927
- MacLeod, C. L., et al. 2010, arXiv:1004.0276
- Malmquist, K. G. 1922, Lund Medd. Ser. I, 100, 1
- Matthews, T. A., & Sandage, A. R. 1963, ApJ, 138, 30
- McDonald, P., & Eisenstein, D. J. 2007, PhRvD, 76, 063009
- Rau, A., et al. 2009, PASP, 121, 1334
- Richards, G. T., et al. 2001, ApJ, 122, 1151
- Richards, G. T., et al. 2006, ApJS, 166, 470
- Richards, G. T., et al. 2009, ApJS, 180, 67
- Rybicki, G. B., & Press, W. H 1994, arXiv:comp-gas/9405004
- Ross, N. P., et al. 2009, ApJ, 697, 1634
- Schmidt, K., et al. 2010, arXiv:1002.2642
- Sesar, B., et al., 2007, AJ, 134, 2236
- Sesar, B., et al. 2010, ApJ, 708, 717
- Schneider, D. P. et al. 2010, AJ, 134, 102
- Schneider, D. P. et al. 2010, arXiv:1004.1167, AJ Accepted

Simonetti, J. H., Cordes, J. M., Heeschen, D. S. 1985, ApJ, 296,

Shen, Y., et al. 2007, AJ, 133, 2222

Shen, Y., et al. 2009, Apj, 697, 1656

Vanden Berk, D. E., et al. 2004, ApJ, 601, 692

Table 3: Source Region Counts from Candidate Quasars Colors

| Color Region | # Known | New (% Known) | New $i \leq 19$ | New $i > 19$ |
|---------------------|---------|-----------------------------|--------------------------|-----------------------------|
| I (white dwarfs) | 5 | 2, <i>1</i> (40%, 20%) | 0, <i>0</i> | 2, <i>1</i> (no previous) |
| II (low- z QSOs) | 5866 | 1387, <i>239</i> (24%, 4%) | 79, <i>34</i> (6%, 2%) | 1308, <i>205</i> (29%, 5%) |
| III (dm/WD) | 134 | 77, <i>47</i> (57%, 35%) | 25, <i>19</i> (50%, 38%) | 52, <i>28</i> (62%, 33%) |
| IV (RR Lyrae) | 158 | 98, <i>62</i> (62%, 39%) | 6, <i>5</i> (25%, 21%) | 92, <i>57</i> (69%, 43%) |
| V (stars) | 252 | 257, <i>210</i> (102%, 83%) | 49, <i>48</i> (80%, 79%) | 208, <i>162</i> (109%, 85%) |
| VI (high- z QSOs) | 158 | 54, <i>36</i> (34%, 23%) | 6, <i>4</i> (16%, 11%) | 48, <i>32</i> (40%, 27%) |

Notes: The color regions I, II, III, IV, V, and VI correspond to the typical location of objects in parentheses in the first column (see Figure 7). Columns 3–5 report the number of new quasars relative to spectroscopically-confirmed quasars, followed after a comma by the number (italicized) of new quasars not already color-selected in Richards et al. (2009) or spectroscopically-confirmed.